Materials Advances

ROYAL SOCIETY OF CHEMISTRY

PAPER

View Article Online
View Journal | View Issue

Cite this: *Mater. Adv.*, 2023, 4, 2332

Understanding the synergistically enhanced thermocatalytic decomposition of ammonium perchlorate using cobalt nanoparticle-embedded nitrogen-doped graphitized carbon†

Hong Lin,[a] Qingchun Zhang,*[ab] Huiyu Liu,[a] Shiying Shen,*[b] Zhiliang Guo,[a] Bo Jin*[a] and Rufang Peng[a]

Ammonium perchlorate (AP) as an oxidizer is widely employed in composite solid propellants (CSPs), and the thermal decomposition kinetics of AP can significantly affect the combustion behavior of CSPs. Therefore, the more apparent specific heat release at lower high-temperature decomposition (HTD) temperature of AP poses a challenge for the development of highly active catalysts.In this work, well-designed synergistic catalysts, cobalt nanoparticle embedded N-doped porous graphitized carbon (Co-NPs@NC), were obtained by straightforward high-temperature pyrolysis of the zeolite imidazolate framework-67 precursor under an argon atmosphere, among which Co-NPs@NC-800 exhibits excellent heat release ability and catalytic activity. The differential thermal analysis results indicated that the HTD temperature and apparent activation energy of AP with Co-NPs@NC-800, respectively, decreased by 133.0 °C and 86.3 kJ mol^{-1}, while the heat release was increased by 5.4 times compared with that of pure AP. The excellent comprehensive properties of Co-NPs@NC-800 are attributed to the high catalytic activity of well-dispersed Co-NPs, the intrinsic adsorption capacity of Co-NPs for NH_3, and the synergistically enhanced effect of N-doped porous graphitized carbon to achieve good electrical conductivity and increase heat release, which facilitate its potential application as a high-efficiency catalyst for the thermocatalytic decomposition of AP.

Received 18th November 2022,
Accepted 16th April 2023

DOI: 10.1039/d2ma01038k

rsc.li/materials-advances

1. Introduction

Composite solid propellants (CSPs) mainly contain a binder (hydroxyl-terminated polybutadiene), a metal fuel (aluminum powder), and an oxidizer (ammonium perchlorate (AP)), of which AP usually accounts for more than half of the CSPs.[1] Moreover, the thermal decomposition kinetics of AP can significantly affect the combustion behavior of CSPs.[2] In general, lower high-temperature decomposition (HTD) temperature and higher heat release of AP can achieve the increase of the combustion rate, high specific impulse, and low-pressure exponent of CSPs.[3,4] In order to enhance the combustion performance of CSPs, the catalytic thermal decomposition of AP was extensively studied *via* utilizing the catalytic activity of nano metals[5–8] and nano metal oxides.[9–14] In contrast to nano metal oxides, the corresponding nano metals have a better ability to catalyze the thermal decomposition of AP,[15–17] mainly because of its special electronic effect of lattice defects[18,19] and oxidation exothermic enhancement effect.[16] Among the nanometals, cobalt nanoparticles (Co-NPs) revealed excellent catalytic performance compared with other nanometals.[19] However, nanometals face the common problems of aggregation and oxidation caused by high surface free energy, resulting in a decrease in catalytic activity and spontaneous combustion or explosion, respectively. To solve these problems, stabilizing the nanoparticles on support materials as an effective strategy is usually adopted.[20] Considering that the heat release of AP can also significantly influence the combustion behavior of CSPs, carbon materials, for instance, carbon nanotubes, graphene, and amorphous carbon, which can not only increase the heat release rate due to its exothermic reaction with oxidizing gas produced by thermal decomposition of AP, but can also reduce the HTD temperature,[21–24] were often selected as the ideal supports to construct nanocomposites[12,25–29] However, these nanocomposites are usually fabricated through a bottom-up method, in which nanoparticles are first prepared and then loaded on.

[a] *State Key Laboratory of Environment-friendly Energy Materials, School of Materials Science and Engineering, Southwest University of Science and Technology, Mianyang 621010, P. R. China.*
E-mail: zhangqingchun@swust.edu.cn, jinbo0428@163.com; Tel: +86-816-2419011
[b] *Institute of Applied Physics and Materials Engineering, University of Macau, Macao SAR, 999078, P. R. China. E-mail: shiyingshen@um.edu.mo*

† Electronic supplementary information (ESI) available. See DOI: https://doi.org/10.1039/d2ma01038k

The bottom-up method is aimed at the realization of efficient dispersion and loading of nanoparticles, but due to the aggregation caused by the higher surface free energy of the smaller-sized nanoparticles, the low surface area of the support, and the lack of strong interactions between nanoparticles and substrates, it cannot be achieved.

Fortunately, metal-organic frameworks (MOFs), especially zeolitic imidazolate frameworks (ZIFs) with ultrahigh surface area, well-defined structure, uniform particle size, and accurate designability, have been sufficiently demonstrated to be promising in catalysis. Metal ions or clusters are periodically distributed in ZIFs, which are suitable for the preparation of nanocomposites using a top-down approach. Hence, ZIFs have been used as precursors and have been converted, *via* high-temperature pyrolysis under an inert atmosphere, to metal nanoparticles or even single-atomic well-dispersed particles, which have been anchored on the resultant N-doped porous graphitized carbon (NC) that partially inherits the characteristics of ZIFs.[30–34]

Therefore, zeolitic imidazolate framework-67 (ZIF-67), as a Co-based MOF material, was rationally used as a precursor to fabricate Co-NPs embedded NC (Co-NPs@NC) catalysts in this work, which may not only realize the catalytic synergistic effect of Co-NPs and NC, but also ensure high catalytic activity and stability of Co-NPs by inhibiting migration and agglomeration. To the best of our knowledge, the thermocatalytic activity of Co-NPs@NC remains unexplored. Herein, detailed characterization of thermocatalytic decomposition of AP is carried out and the catalytic mechanism is discussed.

2. Results and discussion

2.1 Synthesis and characterization

As illustrated in Fig. 1a, the ZIF-67 precursor was fabricated *via* a coordination reaction between $Co(NO_3)_2{\cdot}6H_2O$ and 2-methylimidazole in methanol, and then the ZIF-67 precursor was pyrolyzed under an argon atmosphere at different temperatures (600, 800, and 1000 °C), in which 2-methylimidazole was pyrolyzed to NC, and then Co^{2+} would be reduced by NC to cobalt single atoms (Co-SAs) and most will further aggregate to small size Co-NPs that are embedded on the NC, denoted as Co-NPs@NC-*T*, in which the *T* represents the pyrolysis temperature.

The powder X-ray diffraction (XRD) patterns of the ZIF-67 precursor showed strong and sharp characteristic diffraction peaks and are similar to the XRD patterns obtained from theoretical simulation (Fig. S1a, ESI†). The Fourier-transform infrared (FTIR) spectrum of the ZIF-67 precursor showed a characteristic peak at 431 cm^{-1} for the ν(Co–N); in comparison with 2-methylimidazole the characteristic peak at 1840 cm^{-1} for the ν(N–H) disappeared (Fig. S1b, ESI†) due to the deprotonation and coordination reactions of 2-methylimidazole. The scanning electron microscopy (SEM) images showed clear rhombohedral features with a uniform size of about 1 μm (Fig. 1b). These results indicate that the structure of the ZIF-67 precursor was as we expected.

The SEM and high-resolution transmission electron microscopy (HRTEM) of Co-NPs@NC-800 reveal that the resultant

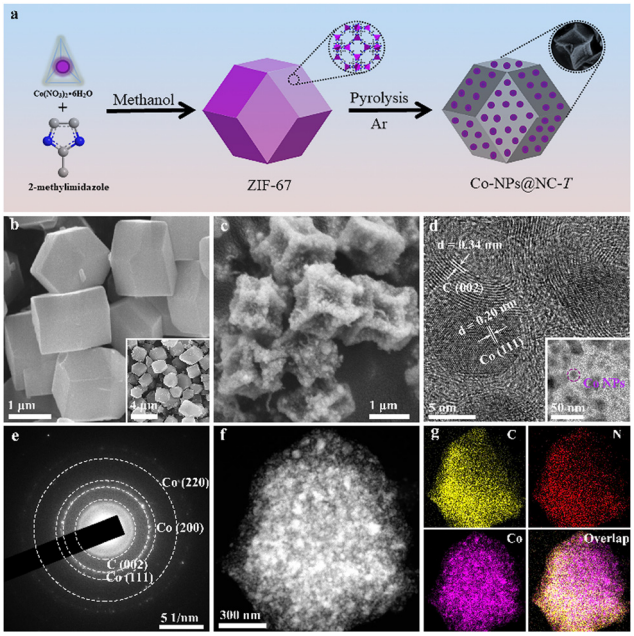

Fig. 1 (a) The schematic illustration of the synthesis of Co-NPs@NC-*T* catalysts. (b) SEM of the ZIF-67 precursor. (c) SEM, (d) HRTEM, (e) SAED pattern, (f) TEM, and (g) TEM elemental mappings of Co-NPs@NC-800.

nanocage has a rhombic dodecahedron shape with a plicated rough surface (Fig. 1c), and the lattice spacings are 0.20 nm and 0.34 nm, corresponding to the (111) plane of Co-NPs and the (002) plane of NC, respectively. The Co-NPs with a uniform size of about 5 nm were completely embedded in the NC layers (Fig. 1d); meanwhile, the strong interaction between the NC and Co-NPs[35–37] resulted in a highly stable structure in Co-NPs@NC-800. Besides, the selected area electron diffraction (SAED) pattern also exhibited the diffraction rings of Co-NPs and NC (Fig. 1e). Moreover, TEM elemental mappings also displayed the uniform distribution of C, N, and Co elements, revealing the successful encapsulation of Co-NPs in NC. Similar morphology and construction are also observed for Co-NPs@NC-600 (Fig. S2, ESI†). By contrast, the morphology of Co-NPs@NC-1000 shows markedly folds and thickened NC shells (Fig. S3a, ESI†) due to the good catalytic activity of Co-NPs for graphitizing carbon-rich 2-methylimidazole during the increasing pyrolytic temperature. In addition, the increase in the pyrolysis temperature causes the sublimation of NC to further increase the Co content, which in turn causes the distance between Co atoms to decrease and agglomeration,[37] resulting in a significant change in the size of Co-NPs in Co-NPs@NC-1000 from a uniform 5 nm to more than 50 nm for Co-NPs@NC-600 and Co-NPs@NC-800 (Fig. 1d and Fig. S2b, c, S3b, c, ESI†).

The XRD patterns showed that Co-NPs@NC-*T* all exhibit characteristic peaks at 44.6°, 51.6°, and 76.2°, which are attributed to the (111), (200), and (220) planes of Co-NPs (Fig. 2a), respectively.[38] It is also worth noting that the full-width at half maximum of the peaks for Co-NPs@NC-*T* has gradually decreased with the increase of pyrolysis temperature, indicating the improved crystallization and larger size of Co-NPs, which are

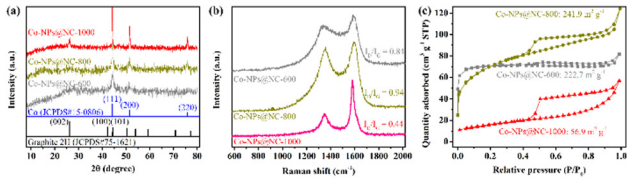

Fig. 2 (a) The XRD patterns, (b) the Raman spectra, and (c) the N_2 adsorption–desorption isotherms of Co-NPs@NC-*T*.

consistent with the results of HRTEM (Fig. 1d and Fig. S2b, S3b, ESI†). In addition, the Co-NPs@NC-1000 compared with Co-NPs@NC-800 and Co-NPs@NC-600 exhibits an additional peak at approximately 26.2° for the (002) crystal plane of graphitized carbon, indicating the higher graphitization degree of carbon with the increase of pyrolysis temperature.[39] The carbon structure in Co-NPs@NC-*T* was further investigated using Raman spectra. The results showed that two characteristic bands located at 1350 cm^{-1} and 1580 cm^{-1} (Fig. 2b) can be assigned to the disordered carbon (D band) and the graphitic carbon (G band),[37] respectively. Generally, the lower relative intensity ratio of the D to G band (I_D/I_G) value indicates a higher degree of graphitization. The I_D/I_G value of Co-NPs@NC-1000 is significantly lower than that of Co-NPs@NC-800 and Co-NPs@NC-600, suggesting the increased degree of graphitization due to the good catalytic activity of Co-NPs produced at a higher pyrolytic temperature for graphitizing carbon-rich 2-methylimidazole during the pyrolytic process,[40,41] which agreed well with the XRD results (Fig. 2a). Moreover, it is also worth noting that the higher graphitization degree of Co-NPs@NC-1000 with an increase in the electrical and thermal conductivity will benefit the thermal decomposition of AP.[42] The specific surface area and porous structure of Co-NPs@NC-*T* were investigated using nitrogen adsorption–desorption isotherms (Fig. 2c). The Co-NPs@NC-600 exhibited a type I isotherm, which displays a significantly increased uptake at a relatively low nitrogen pressure (P/P_0 = 0–0.1) and less obvious hysteresis loop at high nitrogen pressure (P/P_0 = 0.5–0.99), indicating the coexistence of micropores and mesopores.[43] The Co-NPs@NC-800 and Co-NPs@NC-1000 respectively presented the type IV and type V isotherms, which all display obvious hysteresis loop at high nitrogen pressure (P/P_0 = 0.5–0.99) in the main concomitance with micropores. The porous architecture of Co-NPs@NC-*T* has also been verified by pore size distributions (Fig. S4, ESI†). Due to the structural collapse caused by the higher pyrolytic temperature, as expected, the Co-NPs@NC-600 and Co-NPs@NC-800 respectively possesses Brunauer–Emmett–Teller surface areas of 222.7 $m^2 g^{-1}$ and 241.9 $m^2 g^{-1}$, which are much higher than that of Co-NPs@NC-1000 of 56.9 $m^2 g^{-1}$. The large specific surface area coupled with high porosity of Co-NPs@NC-800 would facilitate the exposure of active sites and boost the gas diffusion and mass transport, thus enhancing the thermal catalytic process.

X-ray photoelectron spectroscopy (XPS) was performed to investigate the surface chemical composition and elemental valence states of Co-NPs@NC-*T*. The XPS survey showed that Co-NPs@NC-*T* are mainly composed of C, N, and Co elements (Fig. S5, ESI†). The high-resolution C 1s spectra of Co-NPs@NC-*T* can be deconvoluted into three species (Fig. S6, ESI†), corresponding to the graphitic C (284.4 eV), pyridinic C (285.5 eV), and carbonyl C (over 288.0 eV).[44] The high-resolution N 1s spectra of Co-NPs@NC-*T* changed significantly with the increase of pyrolytic temperature (Fig. S7, ESI†). Among them, the high-resolution N 1s spectra of Co-NPs@NC-600 can be deconvoluted into four species (Fig. S7a, ESI†), corresponding to pyridinic N (398.1 eV), Co-N_n (399.2 eV), pyrrolic N (400.2 eV), and graphitic N (401.8 eV).[45] As the pyrolytic temperature increases, the nitrogen element sublimates and the Co element agglomerates, resulting in the remaining pyridinic N (398.1 eV), Co-N_n (399.2 eV), and pyrrolic N (400.2 eV) of Co-NPs@NC-800 (Fig. S7b, ESI†), and pyridinic N (398.1 eV) and pyrrolic N (400.2 eV) of Co-NPs@NC-1000 (Fig. S7c, ESI†). Due to the spin-orbit coupling, the high-resolution Co 2p spectra of Co-NPs@NC-*T* were divided into two pairs at about 781.0 eV (Co 2p3/2) and 795.0 eV (Co 2p1/2), which were deconvoluted to Co^0 (778.8/793.6 eV), Co^{3+} (780.1/795.9 eV) of Co_2O_3 produced by oxidizing the metal cobalt exposed on the surface by air, and satellite (786.1/804.2 eV).[46,47] Notably, as the pyrolytic temperature increases, the signal of Co^0 relative to Co^{3+} gradually increases (Fig. S8, ESI†), which is consistent with the results of XRD and HRTEM. Since the nitrogen element is not and the Co element is decisive active species that catalyze the thermal decomposition of AP, their content has a significant impact on the catalytic properties. Therefore, the content of the Co element in Co-NPs@NC-*T* was determined by XPS and inductively coupled plasma optical emission spectrometry (ICP-OES). The results of XPS showed that as the pyrolytic temperature increases, the content of Co and N elements in Co-NPs@NC-*T* gradually decreases (Table S1, ESI†), which is mainly due to the Co-NPs catalyzing carbon-rich 2-methylimidazole to form a more highly graphitized and thicker carbon shell on the surface of Co-NPs at a higher pyrolytic temperature. However, XPS is only a characterization of the surface chemical composition of Co-NPs@NC-*T*, and the use of ICP-OES can more accurately measure the overall chemical composition. The results of ICP-OES show that as the pyrolytic temperature increases, the sublimation of carbon is accelerated, and the content of cobalt gradually increases. The content of Co element in Co-NPs@NC-600, Co-NPs@NC-800, and Co-NPs@NC-1000 reached 37.8 wt%, 43.3 wt%, and 56.9 wt% (Table S1, ESI†), respectively.

2.2 Catalytic activity and mechanism

Differential thermal analysis (DTA) was performed to investigate the effect of catalytic activity of Co-NPs@NC-*T* and ZIF-67 on the thermocatalytic decomposition of AP. As we all know, the crystallographic system of AP changes from orthogonality to cubic during heating, which is accompanied by an endothermic peak at 242.7 °C. As the temperature continues to increase, the AP undergoes thermal decomposition accompanied by two violent exothermic peaks, corresponding to low-temperature thermal decomposition (LTD) at about 299.6 °C and HTD at about 430.8 °C, respectively (Fig. S9a, ESI†). Due to the content of catalyst in AP having a significant effect on reducing the HTD

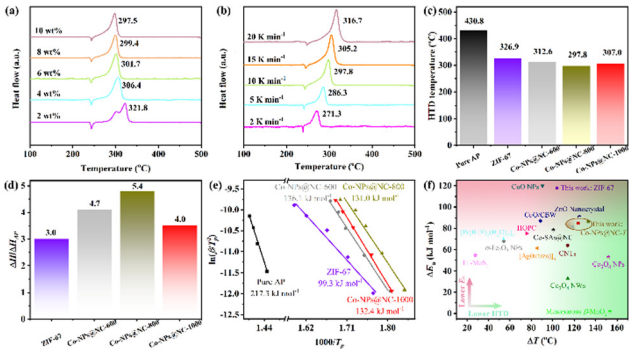

Fig. 3 (a) The DTA curves of AP with different contents of Co-NPs@NC-800 at a heating rate of 10 K min^{-1}. (b) The DTA curves of AP with 10 wt% Co-NPs@NC-800 at different heating rates. (c) The HTD temperature of pure AP and AP with 10 wt% ZIF-67 or Co-NPs@NC-*T* mixture at a heating rate of 10 K min^{-1}. (d) The $\Delta H/\Delta H_{AP}$ (ratio of heat release) of AP with 10 wt% ZIF-67 or Co-NPs@NC-*T* compared with pure AP. (e) The fitting curve dependence of $\ln(\beta/T_p^2)$ on $1000/T_p$ of pure AP and AP with 10 wt% ZIF-67 or Co-NPs@NC-*T* mixture based on the Kissinger method. (f) The comparison of the ΔE_a and ΔT of AP with 10 wt% ZIF-67 or Co-NPs@NC-*T* with reported catalyst/AP mixture in the literature.

temperature,[48,49] the catalytic decomposition process of AP with 2, 4, 6, 8, and 10 wt% Co-NPs@NC-*T* was explored (Fig. 3a and Fig. S9b, c, ESI†). The results indicated that with the increasing content of Co-NPs@NC-*T*, the exothermic peaks of the HTD process are significantly reduced compared with that of pure AP, and even overlap with the LTD process. Considering the uniform dispersion of catalysts Co-NPs@NC-*T* or ZIF-67 in AP, AP with 10 wt% catalysts was chosen for a thermocatalytic decomposition kinetics study by DTA at heating rates 2, 5, 10, 15, and 20 K min^{-1} (Fig. 3b and Fig. S9d–f, ESI†), typically taking a heating rate of 10 K min^{-1} as an example for comparison of catalytic activity. After adding catalysts ZIF-7 and Co-NPs@NC-*T*, the crystal transformation temperature of AP did not change obviously, but the HTD temperature significantly reduced compared with that of pure AP, respectively up to 326.9, 312.6, 297.8, and 307.0 °C (Fig. 3c). The ratio of apparent specific heat release ($\Delta H/\Delta H_{AP}$) obtained according to the HTD peak area of AP with catalyst comparison with pure AP (Table S2, ESI†) remarkably increases, which is 3.0–5.4 times that of pure AP (Fig. 3d). Due to the thermocatalytic decomposition of AP, ZIF-67 needs to undergo an oxidation process, ZIF-67 is first converted to cobalt oxide or chloride embedded NC,[48] where the intrinsic catalytic activity of cobalt oxides or chlorides is lower than that of Co-NPs, while the conversion of 2-methylimidazole in ZIF-67 to NC is an endothermic process. Therefore, ZIF-67 is lower than Co-NPs@NC-*T* in reducing HTD temperature and increasing $\Delta H/\Delta H_{AP}$, as expected. Besides, it should be noted that among the Co-NPs@NC-*T* catalysts, Co-NPs@NC-800 exhibits the best catalytic activity, instead of showing a consistent pattern with pyrolysis temperature. In general, the smaller the size of the metal NPs, the higher the catalytic activity. However, ZIF-67 derived Co-NPs@NC-*T* are mainly composed of NC and Co-NPs, and a higher content of Co-NPs is also beneficial to the improvement of catalytic activity. In this work, as the pyrolytic temperature increases, the size of Co-NPs in Co-NPs@NC-*T* gradually becomes larger (Fig. 1d and Fig. S2b, S3b, ESI†), and the content of Co-NPs increases (Table S1, ESI†). The Co-NPs@NC-800 has a moderate size and content of Co-NPs, and exhibited the best catalytic activity.

In addition, variations in the heating rate can result in significantly different HTD temperatures for the same sample. The faster the heating rate, the significant the HTD peak movement toward a higher temperature, which has a strong correlation with the HTD temperature and the heating rate and can be used for calculating important kinetic parameters based on the Kissinger method (eqn (1)).[56]

$$\ln\left(\frac{\beta}{T_p^2}\right) = \ln\left(\frac{AR}{E_a}\right) - \frac{E_a}{RT_p} \quad (1)$$

where β corresponds to the heating rate (K min^{-1}), E_a is the apparent activation energy (kJ mol^{-1}), T_p is the peak temperature of HTD (K), A is expressed as a pre-exponential factor, and R is an ideal gas constant (8.314 J mol^{-1} K^{-1}). According to eqn (1), a straight line can be described utilizing the linear variation of $\ln(\beta/T_p^2)$ with $1000/T_p$, and the kinetic parameters can be obtained from the slope and the intercept of the straight line, such as A and E_a. The calculated E_a of the pure AP approach is about 217.3 kJ mol^{-1} in the HTD process. Nevertheless, when ZIF-67 and Co-NPs@NC-*T* were introduced into AP, the E_a of AP was significantly decreased to 99.3, 136.1, 131.0, and 132.4 kJ mol^{-1}, respectively (Fig. 3e). Because the HTD temperature and E_a are heavily influenced by the test conditions, a rigorous metric is needed to compare the catalytic activity of different catalysts. In this regard, the ΔT and ΔE_a are the metrics employed, where ΔT and ΔE_a respectively are the differences in the E_a and the HTD temperature between the pure AP and catalyst/AP mixture obtained under consistent test conditions. The higher ΔE_a and ΔT indicate faster decomposition of AP at lower HTD temperatures, leading to better catalytic activity. The ΔT and ΔE_a of Co-NPs@NC-*T* are significantly higher than those of HOPC,[42] CNTs,[22] CuO/CBW,[27] 1T-MoS_2,[60] 2H-MoS_2,[60] α-Fe_2O_3 NPs,[55] Co_3O_4 NPs,[52] $[Pr(BTF)_2(H_2O)_5]_n$,[61] and $[Ag(tntrza)]_n$.[57] The ΔT values of Co-NPs@NC-*T* are significantly lower than those of Co_3O_4 NWs[51] and mesoporous β-MnO_2,[53] but it is the exact opposite for ΔE_a. However, the situation is reversed for ZIF-67 and CuO NPs[54] with Co_3O_4 NWs and β-MnO_2. The catalytic activity of ZnO nanocrystals and Co-NPs@NC-*T* is comparable, but the $\Delta H/\Delta H_{AP}$ value of 1.9 of the ZnO nanocrystal is much lower than the 4.0–5.4 of Co-NPs@NC-*T* (Fig. 3f and Table 1). From a macroscopic point of view, the excellent comprehensive properties of Co-NPs@NC-*T* are attributed to the high catalytic activity of uniformly dispersed Co-NPs and the synergistically enhanced effect of NC to increase heat release and achieve good electrical conductivity.

In order to better understand the high catalytic activity of Co-NPs@NC-*T*, the mechanism of the catalytic decomposition process of AP was analyzed in detail (Fig. 4). The thermal decomposition of pure AP is a multistage process mainly including LTD, stagnation decomposition (SD), and HTD processes.

Table 1 The catalytic properties of various catalysts in the thermal decomposition of AP

Catalysts	Content (wt%)	HTD peak (°C)	ΔT[a] (°C)	ΔE_a[b] (kJ mol^{-1})	$\Delta H/\Delta H_{AP}$[c]	Ref.
ZIF-67[d]	10	326.9	103.9	118.0	3.0	This work
Co-NPs@NC-600[d]	10	312.6	118.2	81.2	4.7	This work
Co-NPs@NC-800[d]	10	297.8	133.0	86.3	5.4	This work
Co-NPs@NC-1000[d]	10	307.0	123.8	84.9	4.0	This work
Co-SAs@NC[e]	10	327.9	100.5	78.3	2.9	50
Co NPs[f]	5	301.7	151.5	—	—	16
Ni NPs[f]	5	335.6	105.0	—	3.7	15
Co_3O_4 NWs	9	278.0	114.0	33.0	1.9	51
Co_3O_4 NPs	5	301.8	152.0	53.0	1.9	52
Mesoporous β-MnO_2[g]	2	273.1	153.2	1.8	4.4	53
CuO NPs	5	331.6	90.4	119.9	1.9	54
α-Fe_2O_3 NPs	5	367.6	54.3	67.9	1.5	55
ZnO nanocrystal	4	272.0	125.0	90.7	1.8	56
CNTs[f]	—	364.2	113.9	63.9	3.2	22
Graphene	10	336.5	69.7	—	3.4	21
Nitrated GO	10	350.0	106.0	—	3.4	23
HOPC	10	365.3	75.6	75.1	8.1	42
CuO/CBW	5	340.8	88.3	86.9	7.2	27
GT-Co	3.2	307.6	101.7	—	1.2	29
$[Ag(tntrza)]_n$[g]	10	335.2	85.5	61.3	—	57
$(CO)_3Mn$-s-Ic′-CoCp*[g]	5	326.0	84.0	—	2.3	58
$[Pr(BTF)_2(H_2O)_5]_n$	10	379.8	54	70.0	—	59
1T-MoS_2	5	405.7	27.7	54.7	10.4	60
2H-MoS_2	5	416.9	16.5	−2.7	—	60

[a] ΔT is the difference of the HTD peak between pure AP and the catalyst/AP mixture obtained with a heating rate of 10 K min^{-1} except as specially marked. [b] ΔE_a is the difference in the apparent activation energy between pure AP and the catalyst/AP mixture. [c] $\Delta H/\Delta H_{AP}$ is the ratio of apparent specific heat release of the catalyst/AP mixture compared with pure AP obtained with a heating rate of 10 K min^{-1} except as specially marked. [d] The $\Delta H/\Delta H_{AP}$ was determined from the ratio of the HTD peak area of the ZIF-67/AP and Co-NPs@NC-*T*/AP mixture compared with pure AP according to the data in Table S2 (ESI). [e] The Co-SAs@NC is denoted as Co@NC in the literature. [f] The HTD peak, ΔT, and $\Delta H/\Delta H_{AP}$ were obtained with a heating rate of 20 K min^{-1}. [g] The HTD peak, ΔT, and $\Delta H/\Delta H_{AP}$ were obtained with a heating rate of 5 K min^{-1}.

For the LTD process, AP mainly undergoes a gas–solid phase reaction, where the intermediate products $HClO_4$ and NH_3 are generated based on the electron transfer from ClO_4^- to NH_4^+, which is generally considered to be one of the controlling steps.[62] The NC and Co-NPs in Co-NPs@NC-*T* respectively with high electrical conductivity and a partially filled 3d orbital can accelerate the electron transfer process to crack the controlling step.[24,48,63–66] In addition, the generated $HClO_4$ and NH_3 are both adsorbed on the AP surface, which has a chance to undergo a redox reaction with each other. However, $HClO_4$ is unstable under LTD temperature conditions and is easily decomposed into O_2, Cl_2, ClO_3, ClO, and H_2O, which can quickly leave the AP surface before oxidizing the adsorbed NH_3. Thus, the NH_3 accumulation on the AP surface consequently inhibits its decomposition. Subsequently, the SD process occurs following the LTD process. As the temperature gradually increased in the HTD process, the NH_3 was desorbed from the AP surface and entered into the gas phase, where it was completely oxidized by the oxidizing gas. For the whole decomposition process of AP mentioned above, the accumulation of NH_3 on the surface of AP was confirmed to be the one of critical factors that inhibit its thermal decomposition.[10] In the DTA curves of AP with Co-NPs@NC-*T*, the HTD process and the LTD process already overlap (Fig. 3b and Fig. S9d, e, ESI†), which indicated the presence of Co-NPs@NC-*T* to eliminate the SD process caused by the accumulation of NH_3 on the surface of AP. The results of the three-dimensional (3D) FTIR spectrum (Fig. 4a) and the corresponding FTIR spectra of gaseous products in the representative temperature range of 230–350 °C (Fig. 4b) show that there is no characteristic N–H bending vibration absorption peak of NH_3 at about 960 cm^{-1} and 930 cm^{-1}, indicating that there is no NH_3 overflow during the violent decomposition of AP.[67,68] Meanwhile, the spin-polarized first-principles DFT calculation was also used to investigate the adsorption and dissociation behaviors of NH_3 on the different planes of Co-NPs in Co-NPs@NC-*T* and CoN_4 sites in Co-SAs@NC. The binding energies of NH_3 on the (111), (200), (220) planes of Co-NPs and CoN_4 sites are −1.046, −0.628, −1.088, and −0.524 eV, respectively (Fig. 4c). And Co-NPs have a higher binding energy of NH_3 than the CoN_4 sites, showing better catalytic activity (Table S3, ESI†). Therefore, there are reasonable reasons to believe that the Co-NPs@NC-*T* can directly capture NH_3 from the AP surface, eliminating the SD process by weakening the accumulation of NH_3 on the AP surface, and exhibiting excellent catalytic activity. In addition, the binding energies of NH_2, NH, and N species for all planes show a gradually decreasing trend (Fig. S10 and S11, ESI†), which indicates the clear trend of dissociation of NH_3, and then the NH_3 dissociated species, protons, and NC react with the adsorbed oxidizing species by Co-NPs[69,70] to generate N_2O (2180–2260 cm^{-1} and 1250–1330 cm^{-1}),[71] NO (1750–1840 cm^{-1}),[72] NO_2 (1560–1650 cm^{-1}),[72] CO_2 (2350 cm^{-1} and 670 cm^{-1}),[67] H_2O (3480–3625 cm^{-1}), and HCl (2685–3025 cm^{-1})[73] (Fig. 4b), while the Co-NPs@NC-*T* gradually oxidize and burn to release heat, which in turn promotes the AP thermocatalytic decomposition process (Fig. 4c). Therefore, the Co-NPs@NC-*T* exhibit excellent catalytic activity in line with expectations.

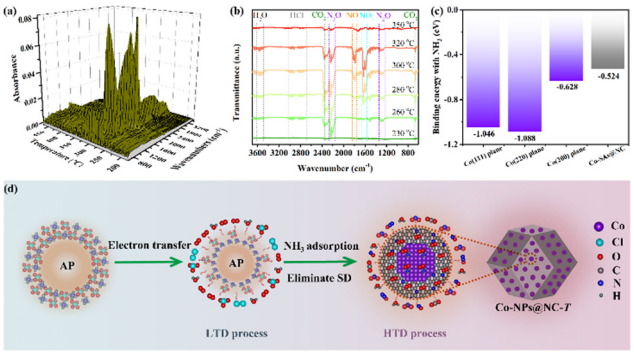

Fig. 4 (a) The 3D FTIR spectrum of gaseous products of themal decomposition of AP with 10 wt% Co-NPs@NC-800 mixture at a heating rate of 10 K min^{-1}. (b) The FTIR spectra of gaseous products during themal decomposition of AP with 10 wt% Co-NPs@NC-800 mixture at representative temperatures. (b) The proposed AP thermocatalytic decomposition mechanism.

3. Conclusions

In summary, Co-NPs@NC-*T* with well-dispersed active species Co-NPs was successfully prepared using a top-down ZIF-67

precursor pyrolysis strategy. The size and content of Co-NPs in Co-NPs@NC-*T* were regulated by adjusting the pyrolysis temperature under an argon atmosphere, and Co-NPs@NC-800 with excellent heat release ability and catalytic activity was obtained. The DTA results indicated that the ΔT and ΔE_a of Co-NPs@NC-800, respectively, reached 133.0 °C and 86.3 kJ mol^{-1}, while the heat release was increased by 5.4 times compared with that of pure AP. The excellent comprehensive properties of Co-NPs@NC-800 are attributed to the high catalytic activity of well-dispersed Co-NPs, the intrinsic adsorption capacity of Co-NPs for NH_3, and the synergistically enhanced effect of NC to achieve good electrical conductivity and increase heat release, which facilitate its potential application as a high-efficiency catalyst for the thermocatalytic decomposition of AP.

Author contributions

Q. C. Zhang and B. Jin conceived and designed the experiments; H. Lin, H. Y. Liu and Z. L. Guo performed the experiments; H. Lin, H. Y. Liu, Z. L. Guo, and R. F. Peng analyzed the data; H. Lin, Q. C. Zhang, and H. Y. Liu wrote and edited the manuscript.

Conflicts of interest

The authors declare no conflict of interest.

Acknowledgements

The authors are grateful for financial support from the Sichuan Science and Technology Program (project no. 2023NSFC0098) and the Project of State Key Laboratory of Environment-friendly Energy Materials, Southwest University of Science and Technology (project no. 21fksy24).

References

1 S. Chaturvedi and P. N. Dave, Solid propellants: AP/HTPB composite propellants, *Arab. J. Chem.*, 2019, **12**(8), 2061–2068.
2 C. Dennis and B. Bojko, On the combustion of heterogeneous AP/HTPB composite propellants: A review, *Fuel*, 2019, **254**, 115646.
3 S. Vyazovkin and C. A. Wight, Kinetics of Thermal Decomposition of Cubic Ammonium Perchlorate, *Chem. Mater.*, 1999, **11**(11), 3386–3393.
4 G. Marothiya, *et al.*, Effects on Burn Rates of Pellets and Propellants with Catalyst-Embedded AP, *J. Propul. Power*, 2018, **34**(4), 969–974.
5 S. Chaturvedi, P. N. Dave and N. N. Patel, Nano-Alloys: Potential Catalyst for Thermal Decomposition of Ammonium Perchlorate, *Synth. React. Inorg., Met.-Org., Nano-Met. Chem.*, 2014, **44**(2), 258–262.
6 S. Chaturvedi and P. N. Dave, A review on the use of nanometals as catalysts for the thermal decomposition of ammonium perchlorate, *J. Saudi Chem. Soc.*, 2013, **17**(2), 135–149.
7 J. K. Sharma, *et al.*, Review on the Catalytic Effect of Nanoparticles on the Thermal Decomposition of Ammonium Perchlorate, *Energy. Environ. Focus.*, 2014, **3**(2), 121–130.
8 P. L. Ríos, *et al.*, Ferrocene-modified dendrimers as support of copper nanoparticles: evaluation of the catalytic activity for the decomposition of ammonium perchlorate, *Mater. Today Chem.*, 2022, **23**, 100631.
9 I. P. S. Kapoor, P. Srivastava and G. Singh, Nanocrystalline Transition Metal Oxides as Catalysts in the Thermal Decomposition of Ammonium Perchlorate, *Propell. Explos. Pyrot.*, 2009, **34**(4), 351–356.
10 L. Zhou, *et al.*, Facet effect of Co_3O_4 nanocatalysts on the catalytic decomposition of ammonium perchlorate, *J. Haz. Mat.*, 2020, **392**, 122358.
11 S. Chaturvedi and P. N. Dave, Nano-metal oxide: potential catalyst on thermal decomposition of ammonium perchlorate, *J. Exp. Nanosci.*, 2012, **7**(2), 205–231.
12 T. Chen, *et al.*, Recent progress on transition metal oxides and carbon-supported transition metal oxides as catalysts for thermal decomposition of ammonium perchlorate, *Def. Technol.*, 2021, **17**(4), 1471–1485.
13 J. Chen, *et al.*, The construction of hierarchical hollow Double-Shelled Co_3O_4 for the enhanced thermal decomposition of Ammonium perchlorate, *Appl. Surf. Sci.*, 2022, **571**, 151342.
14 J. Gaete, *et al.*, Mechanistic Insights into the Thermal Decomposition of Ammonium Perchlorate: The Role of Amino-Functionalized Magnetic Nanoparticles, *Inorg. Chem.*, 2022, **61**(3), 1447–1455.
15 H. Duan, *et al.*, Synthesis of Ni nanoparticles and their catalytic effect on the decomposition of ammonium perchlorate, *J. Mater. Process. Tech.*, 2008, **208**(1), 494–498.
16 H. Duan, *et al.*, Synthesis of Co Nanoparticles and Their Catalytic Effect on the Decomposition of Ammonium Perchlorate, *Chin. J. Chem. Eng.*, 2008, **16**(2), 325–328.
17 X. J. Shen, *et al.*, Facile surfactant-free synthesis of monodisperse Ni particles via a simple solvothermal method and their superior catalytic effect on thermal decomposition of ammonium perchlorate, *New J. Chem.*, 2011, **35**(7), 1403–1409.
18 Z. Jiang, *et al.*, Thermalbehavior of ammonium perchlorate and metal powders of different grades, *J. Therm. Anal. Calorim.*, 2006, **85**(2), 315–320.
19 G. Singh, *et al.*, Nanoparticles of Transition Metals as Accelerants in the Thermal Decomposition of Ammonium Perchlorate, Part 62, *J. Energetic. Mater.*, 2013, **31**(3), 165–177.
20 M. P. Pileni, The role of soft colloidal templates in controlling the size and shape of inorganic nanocrystals, *Nat. Mater.*, 2003, **2**(3), 145–150.
21 X. B. Wang, J. Q. Li and Y. J. Luo, Effect of drying methods on the structure and thermal decomposition behavior of ammonium perchlorate/graphene composites, *Wuli Huaxue Xuebao*, 2013, **29**(10), 2079–2086.

22 P. Cui, *et al.*, Preparation and thermal decomposition behavior of carbon nanotubes/ammonium perchlorate composite particles, *Chin. J. Explos. Propellants*, 2006, **29**(4), 25–28.
23 W. Zhang, *et al.*, Nitrated graphene oxide and its catalytic activity in thermal decomposition of ammonium perchlorate, *Mater. Res. Bull.*, 2014, **50**, 73–78.
24 M. Abdelhafiz, *et al.*, Catalytic action of carbon nanotubes on ammonium perchlorate thermal behavior, *React. Kinet., Mech. Catal.*, 2020, **131**(1), 353–366.
25 S. G. Hosseini, S. Gholami and M. Mahyari, Highly dispersed Ni–Mn bimetallic nanoparticles embedded in 3D nitrogen-doped graphene as an efficient catalyst for the thermal decomposition of ammonium perchlorate, *New J. Chem.*, 2018, **42**(8), 5889–5899.
26 Q. Zhou, *et al.*, Facile Fabrication of Cu-doped Carbon Aerogels as Catalysts for the Thermal Decomposition of Ammonium Perchlorate, *Appl. Organomet. Chem.*, 2020, **34**(8), e5700.
27 T. Zhou, *et al.*, Multichanneled hierarchical porous nanocomposite CuO/carbonized butterfly wing and its excellent catalytic performance for thermal decomposition of ammonium perchlorate, *Appl. Organomet. Chem.*, 2020, **34**(8), e5730.
28 J. Chen, *et al.*, 3D Hierarchically ordered porous carbon entrapped Ni nanoparticles as a highly active catalyst for the thermal decomposition of ammonium perchlorate, *Energ. Mater. Front.*, 2021, **2**(1), 14–21.
29 T. An, *et al.*, Thermal Behavior and Thermolysis Mechanisms of Ammonium Perchlorate under the Effects of Graphene Oxide-Doped Complexes of Triaminoguanidine, *J. Phys. Chem. C*, 2018, **122**(47), 26956–26964.
30 S. Dang, Q.-L. Zhu and Q. Xu, Nanomaterials derived from metal–organic frameworks, *Nat. Rev. Mater.*, 2017, **3**(1), 17075.
31 Y.-Z. Chen, *et al.*, Metal–organic framework-derived porous materials for catalysis, *Coord. Chem. Rev.*, 2018, **362**, 1–23.
32 Y. Chen, *et al.*, Single-Atom Catalysts: Synthetic Strategies and Electrochemical Applications, *Joule*, 2018, **2**(7), 1242–1264.
33 Q.-L. Zhu, *et al.*, Atomically Dispersed Fe/N-Doped Hierarchical Carbon Architectures Derived from a Metal–Organic Framework Composite for Extremely Efficient Electrocatalysis, *ACS Energy Lett.*, 2017, **2**(2), 504–511.
34 X. Xie, *et al.*, Performance enhancement and degradation mechanism identification of a single-atom Co–N–C catalyst for proton exchange membrane fuel cells, *Nat. Catal.*, 2020, **3**(12), 1044–1054.
35 Y.-Z. Chen, *et al.*, From Bimetallic Metal-Organic Framework to Porous Carbon: High Surface Area and Multicomponent Active Dopants for Excellent Electrocatalysis, *Adv. Mater.*, 2015, **27**(34), 5010–5016.
36 S. Liu, *et al.*, Metal–Organic-Framework-Derived Hybrid Carbon Nanocages as a Bifunctional Electrocatalyst for Oxygen Reduction and Evolution, *Adv. Mater.*, 2017, **29**(31), 1700874.
37 Z. Wang, *et al.*, Understanding the Synergistic Effects of Cobalt Single Atoms and Small Nanoparticles: Enhancing Oxygen Reduction Reaction Catalytic Activity and Stability for Zinc-Air Batteries, *Adv. Funct. Mater.*, 2021, **31**(45), 2104735.
38 J. Tang, *et al.*, Synthesis and Electrochemical Characterization of N-Doped Partially Graphitized Ordered Mesoporous Carbon–Co Composite, *J. Phys. Chem. C*, 2013, **117**(33), 16896–16906.
39 Y. Ha, *et al.*, Atomically Dispersed Co-Pyridinic N-C for Superior Oxygen Reduction Reaction, *Adv. Energy Mater.*, 2020, **10**(46), 2002592.
40 X. Ao, *et al.*, Markedly Enhanced Oxygen Reduction Activity of Single-Atom Fe Catalysts via Integration with Fe Nanoclusters, *ACS Nano*, 2019, **13**(10), 11853–11862.
41 Y. He, *et al.*, Single Cobalt Sites Dispersed in Hierarchically Porous Nanofiber Networks for Durable and High-Power PGM-Free Cathodes in Fuel Cells, *Adv. Mater.*, 2020, **32**(46), 2003577.
42 J. Chen, *et al.*, Highly space-confined ammonium perchlorate in three-dimensional hierarchically ordered porous carbon with improved thermal decomposition properties, *Appl. Surf. Sci.*, 2018, **457**, 508–515.
43 G. Chen, *et al.*, Zinc-Mediated Template Synthesis of Fe-N-C Electrocatalysts with Densely Accessible Fe-Nx Active Sites for Efficient Oxygen Reduction, *Adv. Mater.*, 2020, **32**(8), 1907399.
44 X. Li, *et al.*, Cobalt nanoparticles embedded in porous N-rich carbon as an efficient bifunctional electrocatalyst for water splitting, *J. Mater. Chem. A*, 2016, **4**(9), 3204–3209.
45 C. Zhao, *et al.*, Ionic Exchange of Metal-Organic Frameworks to Access Single Nickel Sites for Efficient Electroreduction of CO_2, *J. Am. Chem. Soc.*, 2017, **139**(24), 8078–8081.
46 M. C. Biesinger, *et al.*, Resolving surface chemical states in XPS analysis of first row transition metals, oxides and hydroxides: Cr, Mn, Fe, Co and Ni, *Appl. Surf. Sci.*, 2011, **257**(7), 2717–2730.
47 S. K. Tripathy, *et al.*, Hydrothermal synthesis of single-crystalline nanocubes of Co_3O_4, *Mater. Lett.*, 2008, **62**(6–7), 1006–1009.
48 X. Han, *et al.*, Exploring the Roles of ZIF-67 as an Energetic Additive in the Thermal Decomposition of Ammonium Perchlorate, *Energy Fuels*, 2021, **35**(5), 4447–4456.
49 Z. Guo, *et al.*, A novel metal-organic framework precursor strategy to fabricate sub-micron CuO microspheres for catalytic thermal decomposition of ammonium perchlorate, *Mater. Today Commun.*, 2021, **26**, 102139.
50 H. Liu, *et al.*, Zeolite Imidazolate Frameworks-67 Precursor to Fabricate a Highly Active Cobalt-Embedded *N*-Doped Porous Graphitized Carbon Catalyst for the Thermal Decomposition of Ammonium Perchlorate, *ACS Omega*, 2021, **6**(39), 25440–25446.
51 C. Yu, *et al.*, Shape-controlled syntheses of Co_3O_4 nanowires arrays with excellent catalytic performances upon ammonium perchlorate decomposition, *Mater. Res. Bull.*, 2018, **97**, 483–489.

52 S. G. Hosseini, *et al.*, The effect of average particle size of nano-Co_3O_4 on the catalytic thermal decomposition of ammonium perchlorate particles, *J. Therm. Anal. Calorim.*, 2016, **124**(3), 1243–1254.
53 R. A. Chandru, *et al.*, Exceptional activity of mesoporous β-MnO_2 in the catalytic thermal sensitization of ammonium perchlorate, *J. Mater. Chem.*, 2012, **22**(14), 6536–6538.
54 E. Ayoman and S. G. Hosseini, Synthesis of CuO nanopowders by high-energy ball-milling method and investigation of their catalytic activity on thermal decomposition of ammonium perchlorate particles, *J. Therm. Anal. Calorim.*, 2016, **123**(2), 1213–1224.
55 S. G. Hosseini and E. Ayoman, Synthesis of alpha-Fe2O3 nanoparticles by dry high-energy ball-milling method and investigation of their catalytic activity, *J. Therm. Anal. Calorim.*, 2017, **128**(2), 915–924.
56 G. Tang, *et al.*, ZnO Micro/Nanocrystals with Tunable Exposed (0001) Facets for Enhanced Catalytic Activity on the Thermal Decomposition of Ammonium Perchlorate, *J. Phys. Chem. C*, 2014, **118**(22), 11833–11841.
57 F. Yang, *et al.*, Oxygen-Enriched Metal-Organic Frameworks Based on 1-(Trinitromethyl)-1H-1,2,4-Triazole-3-Carboxylic Acid and Their Thermal Decomposition and Effects on the Decomposition of Ammonium Perchlorate, *ACS Appl. Mater. Interfaces*, 2021, **13**(18), 21516–21526.
58 J. L. Arroyo, *et al.*, Heterobimetallic Catalysts for the Thermal Decomposition of Ammonium Perchlorate: Efficient Burning Rate Catalysts for Solid Rocket Motors and Missiles, *Inorg. Chem.*, 2021, **60**(3), 1436–1448.
59 J. Yan, *et al.*, Cu-MOF derived Cu/Cu_2O/C nanocomposites for the efficient thermal decomposition of ammonium perchlorate, *J. Solid State Chem.*, 2021, **297**, 122060.
60 X. Zhao, *et al.*, Regulating safety and energy release of energetic materials by manipulation of molybdenum disulfide phase, *Chem. Eng. J.*, 2021, **411**, 128603.
61 W. Hao, *et al.*, Lanthanide-nitrogen-rich supramolecular complexes (La Ce Pr): Synthesis, structure, and catalysis for ammonium perchlorate, *J. Solid State Chem.*, 2021, **297**, 122001.
62 V. V. Boldyrev, Thermal decomposition of ammonium perchlorate, *Thermochim. Acta*, 2006, **443**(1), 1–36.
63 Y. Zhang and C. Meng, Facile fabrication of Fe_3O_4 and Co_3O_4 microspheres and their influence on the thermal decomposition of ammonium perchlorate, *J. Alloys Compd.*, 2016, **674**, 259–265.
64 H. Xu, *et al.*, Synthesis and catalytic performance of Co_3O_4 particles with octahedral crystal shape, *Ionics*, 2015, **21**(5), 1495–1500.
65 D. L. Sivadas, *et al.*, Insight into the catalytic thermal decomposition mechanism of ammonium perchlorate, *J. Therm. Anal. Calorim.*, 2019, **138**(1), 1–10.
66 M. D. Garrison, *et al.*, Accelerated Decomposition Kinetics of Ammonium Perchlorate via Conformal Graphene Coating, *Chem. Mater.*, 2021, **33**(24), 9608–9617.
67 J. Madarász and G. Pokol, Comparativeevolved gas analyses on thermal degradation of thiourea by coupled TG-FTIRand TG/DTA-MS instruments, *J. Therm. Anal. Calorim.*, 2007, **88**(2), 329–336.
68 Y. Lu, *et al.*, Insights into thermal behavior and gas evolution characteristics of ZnCP and CdCP by TG-FTIR-GC/MS analysis, *J. Anal. Appl. Pyrolysis*, 2022, **163**, 105495.
69 M. Yan, *et al.*, Trends in water-promoted oxygen dissociation on the transition metal surfaces from first principles, *Phys. Chem. Chem. Phys.*, 2017, **19**(3), 2364–2371.
70 X. Zhang, Z. Lu and Z. Yang, The mechanism of oxygen reduction reaction on CoN_4 embedded graphene: A combined kinetic and atomistic thermodynamic study, *Int. J. Hydrog. Energy*, 2016, **41**(46), 21212–21220.
71 W.-S. Dong, *et al.*, Energetic bimetallic complexes as catalysts affect the thermal decomposition of ammonium perchlorate, *Dalton Trans.*, 2022, **51**(25), 9894–9904.
72 J. F. d S. Petruci, *et al.*, Real-Time and Simultaneous Monitoring of NO, NO_2, and N_2O Using Substrate–Integrated Hollow Waveguides Coupled to a Compact Fourier Transform Infrared (FT-IR) Spectrometer, *Appl. Spectrosc.*, 2019, **73**(1), 98–103.
73 H. J. Park, N. M. Kurien and T. R. Rybolt, Simple Acid Vapor Method for Production of HCl and DCl Gas for IR Spectroscopy, *J. Chem. Educ.*, 2018, **95**(12), 2293–2297.